Stabilized Finite Element Framework for Transient Darcy–Brinkman–Forchheimer Flow Under Local Thermal Non-equilibrium

Rafael C. Moura(✉), Isaac P. Santos, and Lucia Catabriga

Federal University of Espírito Santo, Vitória, ES, Brazil
rafaelcabraldemoura@gmail.com, isaac.santos@ufes.br, luciac@inf.ufes.br

Abstract. Numerical simulation of fluid flow in porous media plays a central role in many scientific and engineering applications. Achieving a proper balance between model complexity and numerical discretization is crucial for computational efficiency. Classical Darcy-based models, however, lose accuracy in high-velocity regimes and in highly porous or permeable media, where viscous and inertial effects become significant. In this work, we consider the transient Darcy–Brinkman–Forchheimer (DBF) model, fully coupled with an energy formulation under Local Thermal Non-Equilibrium (LTNE), thereby providing a consistent extension beyond Darcy flow under mixed-convection conditions. The resulting nonlinear system presents significant challenges, particularly in advection-dominated and non-Darcy regimes. To address these challenges, we propose an efficient stabilized finite element framework based on equal-order linear interpolations for all primitive variables. The formulation combines the Streamline Upwind Petrov–Galerkin (SUPG) and Pressure-Stabilizing Petrov–Galerkin (PSPG) stabilization mechanisms, ensuring numerical stability and pressure–velocity compatibility in a strongly nonlinear transient simulation context. The method is evaluated using benchmark free-flow problems adapted to a porous-media setting and a synthetic fractured porous structure based on a Julia-set fractal geometry. The results demonstrate stable, accurate, and physically consistent solutions across different flow regimes, highlighting the robustness and applicability of the proposed framework to complex transient porous-media problems.

Keywords: Darcy-Brinkman-Forchheimer · Stabilized · SUPG · PSPG · SUPS · LSIC · BDF2 · Finite element · Local Thermal Non-Equilibrium

1 Introduction

Numerical simulation of fluid flow in porous media is central to several scientific and engineering applications, including oil reservoir engineering, geological carbon storage, groundwater hydrology, geothermal systems, and advanced

© The Author(s), under exclusive license to Springer Nature Switzerland AG 2027
O. Gervasi et al. (Eds.): ICCSA 2026 Workshops, LNCS 16761, pp. 39–57, 2027.
https://doi.org/10.1007/978-3-032-30527-5_3

materials processing. The classical mathematical framework relies on conservation of mass, Darcy's law [10], and, when required, the energy conservation equation. Although Darcy-based models are robust and widely implemented in both commercial and academic simulations, their validity is restricted to low-velocity regimes where inertial effects are negligible [29]. In highly porous or permeable formations, particularly in fractured systems or near wells, viscous shear and inertial contributions become significant, leading to deviations from Darcy's law. To address these limitations, several extensions have been proposed in the literature, as discussed in [23]. The Brinkman correction incorporates viscous diffusion effects [6], while the Forchheimer term introduces nonlinear inertial contributions relevant at higher Reynolds number regimes [13]. Together, these modifications yield the Darcy–Brinkman–Forchheimer (DBF) formulation, which can be derived from the volume-averaged Navier–Stokes equations [30] combined with generalized porous drag laws [23]. The DBF model provides a unified continuum framework that can represent creeping, viscous-dominated, and inertia-dominated regimes within a single formulation. This unified description is particularly relevant in fractured porous media and near injection or production wells, where flow transitions between regimes may occur.

Alternative strategies for modeling fractured porous media are extensively documented in the literature [4], including equivalent-porous-media models, dual-porosity, dual-permeability, and discrete-fracture-network (DFN) models. While these methods differ in their structural representation of fractures, the DBF framework is especially attractive in higher-velocity regimes where inertial effects must be explicitly accounted for within a continuum formulation.

When thermal effects are considered, additional modeling challenges arise. In high-velocity regimes or in media with significant solid–fluid heat exchange, the assumption of local thermal equilibrium may no longer hold. Under such conditions, separate energy equations must be introduced for the fluid and solid phases, leading to the Local Thermal Non-Equilibrium (LTNE) formulation. The resulting coupled DBF–LTNE system constitutes a strongly nonlinear, potentially advection-dominated problem. Quadratic nonlinearities arise from the Forchheimer term, whereas high Darcy or Reynolds numbers amplify convective transport, potentially leading to numerical instabilities. Furthermore, increasing physical model fidelity typically increases implementation complexity and computational cost, reinforcing the need for a balanced compromise between physical representativeness and numerical tractability.

Stabilized finite element methods offer an effective strategy for addressing these challenges while preserving implementation simplicity. In particular, the combination of Streamline Upwind Petrov–Galerkin (SUPG) [17], and Pressure Stabilized Petrov–Galerkin (PSPG) [25] techniques enables equal-order interpolation for the velocity and pressure fields, reducing implementation complexity while maintaining numerical robustness. Since the seminal developments in [7,27], SUPG and PSPG formulations have been widely employed in incompressible flow simulations. The combination of SUPG and PSPG is sometimes denoted as the SUPS formulation [9]. Variants of these stabilization approaches have also

been proposed in the literature, which incorporate modifications of stabilization parameters and additional shock-capturing mechanisms [2,18,26,28].

In this work, we investigate a stabilized finite element framework for the transient Darcy–Brinkman–Forchheimer model coupled with the Local Thermal Non-Equilibrium formulation. The present contribution extends our previous work [22] by incorporating a thermal LTNE model, adding a Least-Squares on the Incompressibility Constraint (LSIC) stabilized term, and adopting the second-order backward differentiation BDF2 for time discretization [12]. The proposed approach seeks a balanced compromise between physical model fidelity and numerical implementation complexity, enabling robust simulation of advection-dominated and non-Darcy flows in porous media. The formulation is assessed through a series of adapted benchmark problems, including classical flow configuration and fractured porous structures represented by Julia-set fractal geometry [3,8] which has been applied in the literature for other purposes [14,31].

The remainder of this paper is organized as follows. Section 2 presents the governing equations of the transient Darcy–Brinkman–Forchheimer model coupled with the Local Thermal Non-Equilibrium energy formulation. Section 3 describes the stabilized finite element framework, including the SUPS and LSIC formulations adopted for spatial discretization. Section 4 introduces the numerical applications and benchmark configurations, including verification analyses and representative porous-media flow scenarios. Finally, Sect. 5 summarizes the main conclusions of the present work.

2 Governing Equations

The transient Darcy-Brinkman-Forchheimer model is adopted to describe momentum conservation, while a Local Thermal Non-quilibrium model governs the energy balance in the fluid and porous solid phases. Buoyancy effects are incorporated through the Boussinesq approximation. We consider a viscous, incompressible, transient flow in a porous medium occupying a fixed spatial domain $\Omega \subset \mathbb{R}^2$, with boundary Γ. The space–time domain is denoted by $\Omega_T := \Omega \times (0,T]$ for $T > 0$, with the initial configuration prescribed on $\Omega_0 := \Omega \times \{0\}$, and boundary conditions are defined on $\Gamma_T := \Gamma \times (0,T]$.

In dimensional form, mass conservation for an incompressible fluid with no sources or sink terms is represented by:

$$\nabla \cdot \mathbf{u} = 0 \quad \text{in } \Omega_T, \tag{1}$$

where $\mathbf{u}$ is a bidimensional velocity field. Momentum conservation follows the Darcy–Brinkman–Forchheimer model [23], expressed in terms of the velocity $\mathbf{u}$ and pressure P in Ω_T as

$$\frac{\rho_f}{\phi}\left[\frac{\partial \mathbf{u}}{\partial t} + \nabla\left(\frac{\mathbf{u}\cdot\mathbf{u}}{\phi}\right)\right] + \nabla(P - \rho_f \mathbf{g} y) - \frac{\tilde{\mu}}{\phi}\nabla^2\mathbf{u} + \left(\frac{\mu}{\mathbf{K}} + \frac{c_F \rho_f ||\mathbf{u}||}{\mathbf{K}^{1/2}}\right)\mathbf{u} = \mathbf{0}, \tag{2}$$

where ρ_f and μ represent the fluid density and viscosity, respectively. The rock porosity ϕ is a scalar field, and $\mathbf{K}$ is an isotropic permeability tensor. The parameter $\tilde{\mu}$ accounts for the Brinkman viscous correction [6], and c_F denotes the Forchheimer quadratic drag correction. Finally, the gravitational acceleration vector is given by $\mathbf{g} = [0, -g]$. To account for natural and mixed convection effects, density variations are introduced via the Boussinesq approximation, assuming the linear equation of state $\rho_f = \rho_{f_{ref}}[1 - \beta_T(T_f - T_{f_{ref}})]$, where β_T is the thermal expansion coefficient. Substitution into the momentum equation leads to the modified formulation

$$\begin{aligned} &\rho_{f_{ref}} \left[\frac{1}{\phi} \frac{\partial \mathbf{u}}{\partial t} + \frac{1}{\phi} \nabla \left(\frac{\mathbf{u} \cdot \mathbf{u}}{\phi} \right) \right] + \nabla p - \frac{\tilde{\mu}}{\phi} \nabla^2 \mathbf{u} \\ &+ \frac{\mu}{\mathbf{K}} \mathbf{u} + \frac{c_F \rho_{f_{ref}}}{\mathbf{K}^{1/2}} \|\mathbf{u}\| \mathbf{u} + \rho_{f_{ref}} \beta_T \left(T_f - T_{f_{ref}} \right) \mathbf{e}_g = \mathbf{0} \ \text{ in } \Omega_T, \end{aligned} \tag{3}$$

where p is a modified pressure field incorporating the hydrostatic contribution $\rho_{f_{ref}} \mathbf{g}$. Following the validity discussion in [16], the Boussinesq approximation is used here as a controlled numerical modeling assumption to intentionally enhance buoyancy effects and assess the behavior of the numerical method, rather than as a strict small-temperature-difference approximation.

Heat transfer is modeled using a local thermal non-equilibrium approach, in which fluid and solid matrix temperatures are governed by separate energy equations [23]:

$$(\rho c_p)_f \left(\frac{\partial T_f}{\partial t} + \frac{\mathbf{u}}{\phi} \cdot \nabla T_f \right) = \nabla \cdot (\kappa_f \nabla T_f) + \frac{h}{\phi} (T_s - T_f) + \Phi_v \ \text{ in } \Omega_T, \tag{4}$$

$$(\rho c_p)_s \frac{\partial T_s}{\partial t} = \nabla \cdot (\kappa_s \nabla T_s) + \frac{h}{(1-\phi)} (T_f - T_s) \ \text{ in } \Omega_T. \tag{5}$$

Here, κ_f and κ_s denote the isotropic thermal conductivity tensors of the fluid and solid phases, respectively, and h is the convective heat transfer coefficient. Additionally, we assume that the viscous dissipation is neglected, i.e., $\Phi_v = \mathbf{0}$.

For numerical and physical interpretation purposes, the system is nondimensionalized using characteristic length, velocity, pressure, and temperature scales. The resulting formulation is expressed in terms of Reynolds (Re), Darcy (Da), Prandtl (Pr), Nusselt (Nu), and Richardson (Ri)numbers, appropriate for mixed convection regimes:

$$\mathbf{x}^* = \frac{\mathbf{x}}{L_{ref}}, \ \mathbf{t}^* = \frac{U_{ref}\, t}{L_{ref}}, \ \mathbf{u}^* = \frac{\mathbf{u}}{U_{ref}}, \ p^* = \frac{p}{\rho_{ref} U_{ref}^2}, \ T^* = \frac{T - T_{ref}}{\Delta T}, \tag{6}$$

where $\Delta T = T_{hot} - T_{cold}$ and $T_{ref} = (T_{hot} + T_{cold})/2$. For simplicity, the same notation is retained for the dimensionless primitive variables ($\mathbf{u}$, p, T_f, T_s). The resulting dimensionless primitive variable formulation is defined by

$$\nabla \cdot \mathbf{u} = \mathbf{0} \quad \text{in } \Omega_T, \tag{7}$$

$$\frac{\partial \mathbf{u}}{\partial t} + (\mathbf{u}\cdot\nabla)\left(\frac{\mathbf{u}}{\phi}\right) - \left(\frac{\Lambda_u}{Re}\right)\nabla^2\mathbf{u} + \phi\left(\frac{1}{Re\,Da} + \frac{c_F\,\|\mathbf{u}\|}{Da^{1/2}}\right)\mathbf{u} + \phi\,\nabla p + \phi\,Ri\,T_f\,\mathbf{e}_g = \mathbf{f}_u \quad \text{in } \Omega_T, \tag{8}$$

$$\frac{\partial T_f}{\partial t} + \frac{1}{\phi}\mathbf{u}\cdot\nabla T_f - \frac{1}{Re}\nabla\cdot\left(\frac{1}{Pr}\nabla T_f\right) - \frac{Nu}{Re\,Pr\,\phi}(T_s - T_f) = f_{T_f} \text{ in } \Omega_T, \tag{9}$$

$$\frac{\partial T_s}{\partial t} - \frac{1}{Re\,\Lambda_{\rho c_p}}\nabla\cdot\left(\frac{\Lambda_\kappa}{Pr}\nabla T_s\right) - \frac{Nu}{RePr\Lambda_{\rho c_p}(1-\phi)}(T_f - T_s) = f_{T_s} \text{ in } \Omega_T, \tag{10}$$

where $\Lambda_\mu = \tilde{\mu}/\mu$, $\Lambda_\kappa = \kappa_s/\kappa_f$, $\Lambda_{\rho c_p} = (\rho c_p)_s/(\rho c_p)_f$ and $\mathbf{e_g} = [0, -1]$. Source terms $\mathbf{f_u}$, f_{T_f}, and f_{T_s} are introduced when required for verification through manufactured analytical solutions. Initial conditions are prescribed for each primitive variable ψ in the form

$$\psi(\mathbf{x}, 0) = \psi_0(\mathbf{x}) \text{ in } \Omega_0, \tag{11}$$

and the boundary Γ is decomposed in Dirichlet and Neumann portions according to the field variable under consideration, such that $\Gamma = \Gamma_\psi^D \cup \Gamma_\psi^N$ with $\Gamma_\psi^D \cap \Gamma_\psi^N = \emptyset$. The corresponding space–time boundaries are defined over Γ_T, leading to

$$\psi(\mathbf{x}, t) = g_\psi(\mathbf{x}, t) \text{ in } \Gamma_\psi^D \text{ and } \nabla\psi(\mathbf{x}, t)\cdot\mathbf{n} = 0 \text{ in } \Gamma_\psi^N \quad \forall t \in (0, T]. \tag{12}$$

The Neumann boundary conditions are naturally incorporated into the weak formulation through the boundary terms arising from integration by parts. For the scalar pressure field p, no Neumann condition is prescribed.

3 Stabilized Finite Element Formulation

To ensure numerical stability and robustness in advection-dominated and non-Darcy flow regimes, we adopt a stabilized finite element formulation based on equal-order linear interpolations for all primitive variables. The proposed approach combines the SUPG and PSPG techniques with an LSIC stabilization. This unified strategy enables the use of continuous linear elements for both velocity and pressure fields while controlling spurious oscillations, enhancing pressure stability, and improving mass conservation in strongly nonlinear transient regimes. The domain Ω is approximated by a conforming triangulation Ω^h, composed of a finite set of non-overlapping triangular elements Ω_e, such that

$$\Omega^h = \bigcup_{e=1}^{n_e} \Omega_e, \qquad \Omega_i^\circ \cap \Omega_j^\circ = \emptyset \quad \text{for } i \neq j, \tag{13}$$

where Ω_e° denotes the interior of the element Ω_e, n_e is the number of elements in discretized domain Ω^h. Over this partition, finite-dimensional subspaces of

$H^1(\Omega)$ are constructed using continuous piecewise linear polynomials. The finite element approximation space for a generic primitive variable ψ is defined as:

$$\mathcal{H}^{1h} = \{\psi^h \,|\, \psi^h \in \mathcal{C}^0(\Omega), \psi^h|_{\Omega_e} \in \mathcal{P}^1(\Omega_e), \forall \Omega_e \in \Omega^h\}, \tag{14}$$

where $\mathcal{P}^1(\Omega_e)$ denotes the space of first-order polynomials defined on Ω_e. For a generic primitive variable ψ, the corresponding trial and test spaces are defined, respectively, as

$$\mathcal{S}_\psi^h = \{\psi^h \,|\, \psi^h \in [\mathcal{H}^{1h}(\Omega^h)]^d,\ \psi^h = \bar{\psi} \text{ on } \Gamma^D\}, \tag{15}$$

$$\mathcal{V}_\psi^h = \{w_\psi^h \,|\, w_\psi^h \in [\mathcal{H}^{1h}(\Omega^h)]^d,\ w_\psi^h = 0 \text{ on } \Gamma^D\}. \tag{16}$$

where $d = 2$ for the velocity field and $d = 1$ for scalar variables, and $\bar{\psi}$ denotes the prescribed Dirichlet boundary value of ψ on Γ^D.

Since equal-order interpolation is adopted for velocity and pressure fields, the resulting discrete formulation does not satisfy the classical inf-sup (Ladyzhenskaya–Babuška–Brezzi) stability condition [5]. This issue is addressed through the Pressure-Stabilizing Petrov–Galerkin (PSPG) stabilization, which ensures stability of the pressure approximation while allowing the use of continuous linear elements for all primitive variables.

The semidiscrete variational formulation consists of finding the discrete primitive variables $\psi^h \in \mathcal{S}_\psi^h$ for $t \in (0, T]$ such that $\forall\, w_\psi^h \in \mathcal{V}_\psi^h$, the weak form of each balance equation is satisfied. The resulting variational statements for mass, momentum, and energy conservation are described as follows. The Galerkin formulation of the conservation of mass equation onto the discrete space defined over Ω reads

$$\int_\Omega w_p^h \left(\nabla \cdot \mathbf{u}^h\right) d\Omega = 0. \tag{17}$$

The stabilized Petrov–Galerkin formulation adopted for the conservation of momentum combines SUPG, PSPG, and LSIC contributions and is written as

$$\begin{aligned} &\int_\Omega \mathbf{w}_u^h \cdot \mathcal{L}_m^h d\Omega + \sum_{e=1}^{n_e} \int_{\Omega_e} \tau_S (\mathbf{u}^h \cdot \nabla)\mathbf{w}_u^h \cdot \mathcal{L}_m^h d\Omega_e \\ &+ \sum_{e=1}^{n_e} \int_{\Omega_e} \tau_P \nabla w_p^h \cdot \mathcal{L}_m^h d\Omega_e + \sum_{e=1}^{n_e} \int_{\Omega_e} \tau_L (\nabla \cdot \mathbf{w}_u^h)(\nabla \cdot \mathbf{u}^h) d\Omega_e = \mathbf{0}, \end{aligned} \tag{18}$$

where

$$\begin{aligned} \mathcal{L}_m^h(\mathbf{u}^h, p^h, T_f^h) = \frac{\partial \mathbf{u}^h}{\partial t} + (\mathbf{u}^h \cdot \nabla)\left(\frac{\mathbf{u}^h}{\phi}\right) - \left(\frac{\Lambda_\mu}{Re}\right)\nabla^2 \mathbf{u}^h \\ + \phi\left(\tfrac{1}{ReDa} + \tfrac{c_F \|\mathbf{u}^h\|}{Da^{1/2}}\right)\mathbf{u}^h + \phi \nabla p^h + \phi\, Ri\, T_f^h\, \mathbf{e}_g - \mathbf{f}_u. \end{aligned} \tag{19}$$

The element-level stabilization parameters for SUPG, PSPG, and LSIC follow the adaptation proposed in [11] for the Darcy–Brinkman–Forchheimer formula-

tion and are computed as

$$\tau_S = \left\{ \left(\frac{1}{\Delta t}\right)^2 + \left(\frac{2\|\mathbf{u}_b\|}{h_e}\right)^2 + 9\left(\frac{4\Lambda_\mu}{Re\, h_e^2}\right)^2 + \left[\phi\left(\frac{1}{Re\, Da} + \frac{c_F\|\mathbf{u}_b\|}{Da^{1/2}}\right)\right]^2 \right\}^{-1/2}, \tag{20}$$

with $\tau_P = \tau_L = \tau_S$. Here, $\|\mathbf{u}_b\|$ denotes the Euclidean norm of the velocity evaluated at the element barycenter, and $h_e = 4A_e/\pi$ represents the equivalent element size computed from the element area A_e.

For the energy equations of the fluid and solid phases, a Petrov–Galerkin formulation with SUPG stabilization is employed for the fluid equation, while the solid equation retains the standard Galerkin form:

$$\int_\Omega w^h_{T_f} \mathcal{L}^h_{T_f} d\Omega + \sum_{e=1}^{n_e} \int_{\Omega_e} \tau_{S_{T_f}} (\mathbf{u}^h \cdot \nabla) w^h_T \mathcal{L}^h_{T_f} d\Omega_e = 0, \tag{21}$$

$$\int_\Omega w^h_{T_s} \left[\frac{\partial T^h_s}{\partial t} - \frac{1}{Re\, \Lambda_{\rho c_p}} \nabla \cdot \left(\frac{\Lambda_\kappa}{Pr} \nabla T^h_s \right) - \frac{Nu(T^h_f - T^h_s)}{RePr\, \Lambda_{\rho c_p}(1-\phi)} - f_{T_s} \right] = 0 \tag{22}$$

where

$$\begin{aligned} \mathcal{L}^h_{T_f}(\mathbf{u}^h, T^h_f, T^h_s) = \frac{\partial T^h_f}{\partial t} + \frac{\mathbf{u}^h_f}{\phi} \cdot \nabla T^h_f - \frac{1}{Re} \nabla \cdot \left(\frac{1}{Pr_f} \nabla T^h_f \right) \\ - \frac{Nu(T^h_s - T^h_f)}{RePr_f \phi} - f_{T_f}, \end{aligned} \tag{23}$$

and a similar SUPG stabilization parameter adapted from [11]:

$$\tau_{S_{T_f}} = \left[\left(\frac{1}{\Delta t}\right)^2 + \left(\frac{2\|\mathbf{u}_b\|}{h_e}\right)^2 + 9\left(\frac{4}{Re\, Pr\, h_e^2}\right)^2 + \left(\frac{Nu}{Re\, Pr\, \phi}\right)^2 \right]^{-1/2}. \tag{24}$$

The spatial discretization in terms of nodal unknows ($\mathbf{U}$, $\mathbf{P}$, $\mathbf{T}_f$ and $\mathbf{T}_s$) is obtained by restricting the weak forms, Eqs. (18), (21), and (22), to each element Ω_e, which leads to element-level matrices associated with the corresponding contributions of each term. The momentum Eq. (18) generates the standard Galerkin matrices (denoted by superscript G), which, combined with SUPG (S superscript) and LSIC (L superscript) stabilization terms, produce the first block of the discrete momentum equations. The resulting element matrices contributing to the nonlinear coupled system are indicated with overbraces in the expression below:

$$\begin{aligned} \overbrace{(\mathbf{M}^{\mathbf{G}}_{\mathbf{u}} + \mathbf{M}^{\mathbf{S}}_{\mathbf{u}})}^{\mathbf{M_u}} \dot{\mathbf{U}} + \overbrace{(\mathbf{A}^{\mathbf{G}}_{\mathbf{u}}(\mathbf{u}) + \mathbf{A}^{\mathbf{S}}_{\mathbf{u}}(\mathbf{u}) + \mathbf{D}^{\mathbf{G}}_{\mathbf{u}} + \mathbf{R}^{\mathbf{G}}_{\mathbf{u}} + \mathbf{R}^{\mathbf{S}}_{\mathbf{u}} + \mathbf{K}^{\mathbf{L}}_{\mathbf{u}})}^{\mathbf{K_u}} \mathbf{U} \\ + \underbrace{(\mathbf{G}^{\mathbf{G}}_{\mathbf{u}} + \mathbf{G}^{\mathbf{S}}_{\mathbf{u}})}_{\mathbf{G_u}} \mathbf{P} + \underbrace{(\mathbf{R}^{\mathbf{G}}_{\mathbf{T_f}} + \mathbf{R}^{\mathbf{S}}_{\mathbf{T_f}})}_{\mathbf{R_{T_f}}} \mathbf{T}_f = \underbrace{\mathbf{F}^{\mathbf{G}}_{\mathbf{u}} + \mathbf{F}^{\mathbf{S}}_{\mathbf{u}}}_{\mathbf{F_u}}. \end{aligned} \tag{25}$$

The discretized continuity equation, combined with PSPG stabilization (superscript P), introduces additional pressure-coupling terms arising from the momentum residual, yielding the second block of equations:

$$\mathbf{M}_{\mathbf{u}}^{\mathbf{P}}\dot{\mathbf{U}} + \overbrace{(\mathbf{G}_{\rho}^{\mathbf{G}} + \mathbf{A}_{\mathbf{u}}^{\mathbf{P}}(\mathbf{u}) + \mathbf{R}_{\mathbf{u}}^{\mathbf{P}})}^{\mathbf{G}_{\rho}}\mathbf{U} + \mathbf{G}_{\mathbf{u}}^{\mathbf{P}}\mathbf{P} + \mathbf{R}_{\mathbf{T_f}}^{\mathbf{P}}\mathbf{T}_f = \mathbf{F}_{\mathbf{u}}^{\mathbf{P}}. \tag{26}$$

The third block corresponds to the discretization of the local thermal non-equilibrium model. It includes both Galerkin and SUPG contributions for the fluid temperature equation and standard Galerkin terms for the solid temperature equation. The resulting element-level thermal system is given by

$$\begin{aligned}\overbrace{(\mathbf{M}_{\mathbf{T}}^{\mathbf{G}} + \mathbf{M}_{\mathbf{T_f}}^{\mathbf{S}})}^{\mathbf{M}_{\mathbf{T_f}}}\dot{\mathbf{T}}_f + \overbrace{(\mathbf{A}_{\mathbf{T_f}}^{\mathbf{G}}(\mathbf{u}) + \mathbf{A}_{\mathbf{T_f}}^{\mathbf{S}}(\mathbf{u}) + \mathbf{D}_{\mathbf{T_f}}^{\mathbf{G}} + \mathbf{R}_{\mathbf{T_f}}^{\mathbf{G}} + \mathbf{R}_{\mathbf{T_{f,f}}}^{\mathbf{S}})}^{\mathbf{K}_{\mathbf{T_f}}}\mathbf{T}_f \\ + \underbrace{(\mathbf{R}_{\mathbf{T_{s,f}}}^{\mathbf{G}} + \mathbf{R}_{\mathbf{T_{s,f}}}^{\mathbf{S}})}_{\mathbf{R}_{\mathbf{T_{s,f}}}}\mathbf{T}_s = \underbrace{\mathbf{F}_{\mathbf{T_f}}^{\mathbf{G}} + \mathbf{F}_{\mathbf{T_f}}^{\mathbf{S}}}_{\mathbf{F}_{\mathbf{T_f}}},\end{aligned} \tag{27}$$

$$\mathbf{M}_{\mathbf{s}}^{\mathbf{G}}\dot{\mathbf{T}}_s + \overbrace{(\mathbf{D}_{\mathbf{T_s}}^{\mathbf{G}} + \mathbf{R}_{\mathbf{T_{s,s}}}^{\mathbf{G}})}^{\mathbf{K}_{\mathbf{T_s}}^{\mathbf{G}}}\mathbf{T}_s + \mathbf{R}_{\mathbf{T_{f,s}}}^{\mathbf{G}}\mathbf{T}_f = \mathbf{F}_{\mathbf{T_s}}^{\mathbf{G}}. \tag{28}$$

After stacking the corresponding element matrices, the fully coupled element-level system assumes the compact block structure, given by

$$\overbrace{\begin{bmatrix}\mathbf{M_u} & \mathbf{0} & \mathbf{0} & \mathbf{0}\\ \mathbf{M}_{\mathbf{u}}^{\mathbf{P}} & \mathbf{0} & \mathbf{0} & \mathbf{0}\\ \mathbf{0} & \mathbf{0} & \mathbf{M_{T_f}} & \mathbf{0}\\ \mathbf{0} & \mathbf{0} & \mathbf{0} & \mathbf{M}_{\mathbf{T_s}}^{\mathbf{G}}\end{bmatrix}}^{\mathcal{M}_e}\overbrace{\begin{bmatrix}\dot{\mathbf{U}}\\ \dot{\mathbf{P}}\\ \dot{\mathbf{T}}_{\mathbf{f}}\\ \dot{\mathbf{T}}_{\mathbf{s}}\end{bmatrix}}^{\dot{\mathcal{U}}_e} + \overbrace{\begin{bmatrix}\mathbf{K_u} & \mathbf{G_u} & \mathbf{R_{T_f}} & \mathbf{0}\\ \mathbf{G}_{\rho} & \mathbf{G}_{\mathbf{u}}^{\mathbf{P}} & \mathbf{R}_{\mathbf{T_f}}^{\mathbf{P}} & \mathbf{0}\\ \mathbf{0} & \mathbf{0} & \mathbf{K_{T_f}} & \mathbf{R_{T_{s,f}}}\\ \mathbf{0} & \mathbf{0} & \mathbf{R}_{\mathbf{T_{f,s}}}^{\mathbf{G}} & \mathbf{K}_{\mathbf{T_s}}^{\mathbf{G}}\end{bmatrix}}^{\mathcal{K}_e}\overbrace{\begin{bmatrix}\mathbf{U}\\ \mathbf{P}\\ \mathbf{T_f}\\ \mathbf{T_s}\end{bmatrix}}^{\mathcal{U}_e} = \overbrace{\begin{bmatrix}\mathbf{F_u}\\ \mathbf{F}_{\mathbf{u}}^{\mathbf{P}}\\ \mathbf{F_{T_f}}\\ \mathbf{F}_{\mathbf{T_s}}^{\mathbf{G}}\end{bmatrix}}^{\mathcal{F}_e}. \tag{29}$$

In this notation, the zero blocks in Eq. (29) represent submatrices with appropriate dimensions required for the assembly procedure. The element-level contributions provide the mass, stiffness, and source terms that are assembled into the global nonlinear system of Ordinary Differential Equations (ODEs):

$$\mathcal{M}\dot{\mathcal{U}} + \mathcal{K}(\mathcal{U})\mathcal{U} = \mathcal{F}, \tag{30}$$

with:

$$\mathcal{M} = \mathop{\mathbf{A}}_{e=1}^{n_e}\mathcal{M}_e, \quad \mathcal{K} = \mathop{\mathbf{A}}_{e=1}^{n_e}\mathcal{K}_e \quad \text{and} \quad \mathcal{F} = \mathop{\mathbf{A}}_{e=1}^{n_e}\mathcal{F}_e. \tag{31}$$

Time integration is performed using the second-order Backward differentiation method (BDF2), described in [12]. The semi-discrete system of ODEs (30) can be written as

$$\left(\frac{3}{2}\mathcal{M} + \Delta t\mathcal{K}^{n+1}\right)\mathcal{U}^{n+1} = \mathcal{M}\left(2\mathcal{U}^{n} - \frac{1}{2}\mathcal{U}^{n-1}\right) + \Delta t\mathcal{F}^{n+1}, \tag{32}$$

where Δt denotes the time step. Owing to the nonlinear dependence of the stiffness matrix $\mathcal{K}(\mathcal{U})$, a lagged linearization strategy based on the previous time level is employed, combined with a Picard iterative scheme. At each nonlinear iteration, a linearized system is solved using GMRES, preconditioned with an incomplete LU factorization. The iterative process continues until the norm of the nonlinear residual falls below a prescribed tolerance or the maximum number of nonlinear iterations is reached.

4 Numerical Applications

Numerical applications of the Darcy–Brinkman–Forchheimer model with local thermal non-equilibrium often explore idealized configurations and adopt nondimensional parameter ranges tailored to specific theoretical objectives. In the present work, however, the analysis is oriented toward scenarios arising in petroleum engineering. Nevertheless, because the formulation assumes incompressibility, the examples considered here represent simplified abstractions of realistic reservoir conditions. To ensure that the selected application remains within physically grounded magnitudes for the dimensionless groups, the primitive variables are scaled using representative thermophysical properties of the fluid and rock matrix evaluated at characteristic reference conditions. This approach allows the nondimensional groups governing the system to attain realistic magnitudes while preserving mathematical consistency. All results in the following sections are reported in dimensionless variables.

The working fluid is water at standard conditions (298 K and 1 atm) [20]. Its thermophysical properties are summarized in Table 1. The thermal expansion coefficient was obtained from isobaric density data using a second-order centered finite-difference approximation.

Table 1. Thermophysical properties of water at 298 K and 1 atm.

ρ_f	μ	c_p	κ_f	β_T	Pr
$\mathrm{kg/m^3}$	$\mathrm{Pa \cdot s}$	$\mathrm{kJ/(kg\,K)}$	$\mathrm{W/(m\,K)}$	$\mathrm{1/K}$	-
997.09	8.9307×10^{-4}	4.1814	0.60627	3.0×10^{-4}	6.16

Two synthetic porous media are considered in the applications to represent contrasting reservoir characteristics. Rock Type A corresponds to a lower-permeability sandstone-like formation, while Rock Type B represents a highly permeable fractured karst limestone-like structure. The adopted porosity, permeability, and thermal properties are given in Table 2, with values based on ranges reported in [24]. Permeability values are expressed in Darcy and converted to SI units using $1\mathrm{D} = 9.869 \times 10^{-13}, \mathrm{m}^2$ and $c_F(\phi) = 1.8/(\phi^{1.5}\sqrt{180})$ following modified Ergun [1,21].

The interphase heat transfer coefficient appearing in the energy Eqs. (9) and (10) is expressed through the Nusselt number, computed using the correlation

Table 2. Representative thermophysical properties of reference porous media.

Type	ϕ %	k D	c_F -	κ_s W/(m K)	ρ_s kg/m^3	c_p kJ/(kg K)	Λ_κ -	$\Lambda_{\rho c_p}$ -
A	50	0.1	0.38	4.1	2.35×10^3	1.64	6.76	0.92
B	80	1000	0.19	3.0	2.50×10^3	0.93	4.95	0.56

presented in [19]. In the present study, an adapted version is employed, replacing the original characteristic Reynolds number Re_D with the pore-scale Reynolds number $Re_k = \rho_f \mathbf{u}\sqrt{k}/\mu$ and $Pr = (\mu\, c_p)/\kappa_f$:

$$Nu = f(Re_k, Pr, \phi) = \left(1 + \frac{4(1-\phi)}{\phi}\right) + \frac{1}{2}(1-\phi)^{1/2} Re_k^{0.6} Pr^{1/3}. \tag{33}$$

Due to scale separation $L \gg \sqrt{k}$, the flow regimes are characterized in terms of Re_k, which governs inertial effects at the pore scale. For each application, a target Reynolds number is prescribed. The corresponding reference velocity is then computed from fluid properties, allowing evaluation of both Re_k and Ri. These parameters are verified to ensure consistency with the intended flow regime. The temperatures T_{hot}, T_{cold}, and length scale L_{ref} are selected according to the specific application scenario. In all numerical applications, the Brinkman factor in the momentum Eq. (8) is fixed as $\Lambda_\mu = 1$.

4.1 Numerical Solver Verification

To verify the numerical implementation, a manufactured analytical solution is considered. The primitive variables $\mathbf{u}$, p, T_f, and T_s are defined in the domain $\Omega = [0, 20] \times [0, 4]$ as

$$\mathbf{u} = \left[1 - \left(\frac{y-2}{2}\right)^2, 0\right], \quad p = 3 - \frac{x}{10} \quad \text{and} \quad T_f = T_s = 2 - \frac{x}{20}. \tag{34}$$

Substituting these expressions into Eqs. (7)–(10), the forcing terms $\mathbf{f}_\mathbf{u}$, f_{T_f}, and f_{T_s} are obtained so that the analytical solution fields satisfy the governing equations. The forcing terms were computed by setting Re, Da, c_F, Pr, Nu, Ri, Λ_μ, Λ_κ, and $\Lambda_{\rho c_p}$ to unity, with porosity $\phi = 0.5$. In the numerical experiment, a porous-channel domain is considered in which the primitive variables are prescribed on the boundary, while the initial conditions are set to zero. The domain is discretized using a structured alternating triangular mesh with 1377 nodes and 2560 elements, generated using the Gmsh Julia API [15] and a dimensionless time step of $\Delta t = 1$. Figure 1 shows the recovered steady-state fields, and Table 3 reports the corresponding L_2 error.

The numerical solution accurately reproduces the expected analytical solution fields. The main deviation appears in the pressure solution, as expected given the use of equal-order linear interpolation for velocity and pressure.

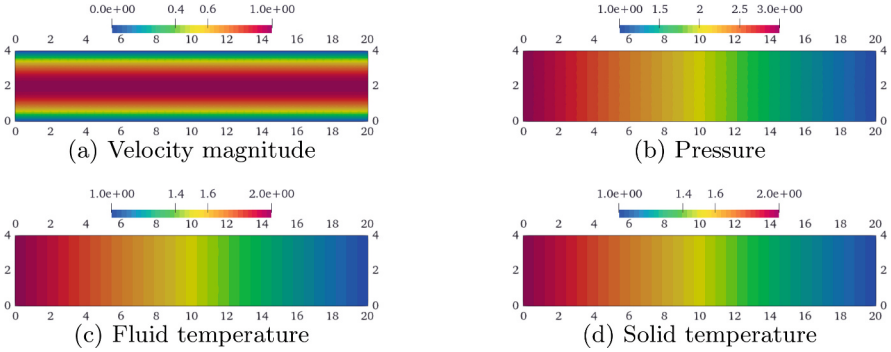

Fig. 1. Numerical solutions of the solver verification problem at $t = 41$.

Table 3. L_2 norms of error $e^{\psi}_{L_2} = \|\psi^h - \psi\|_{L_2}$.

$\|u_x^h - u_x\|_{L_2}$	$\|u_y^h - u_y\|_{L_2}$	$\|p^h - p\|_{L_2}$	$\|T_f^h - T_f\|_{L_2}$	$\|T_s^h - T_s\|_{L_2}$
6.29×10^{-3}	1.97×10^{-4}	1.12×10^{-2}	6.40×10^{-5}	4.77×10^{-5}

4.2 Differentially Heated Porous Cavity

Figure 2 shows the porous media version of a classical benchmark for thermal flow applications. The problem consists of a heated cavity with two insulated walls: top and bottom. Different temperatures are fixed on the left and right walls, creating a thermal gradient that, driven by the thermal buoyancy, induces natural convection within the porous cavity.

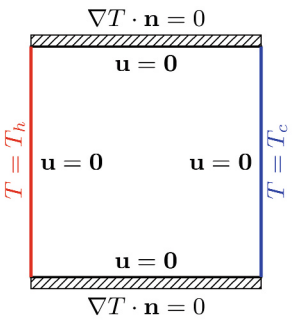

(a) Geometry and boundary conditions

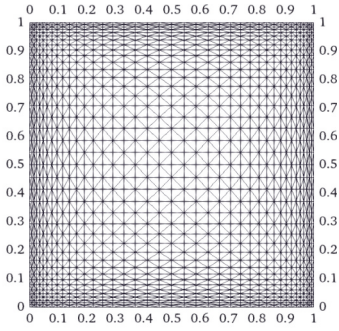

(b) Finite element mesh

Fig. 2. Heated porous cavity benchmark.

The solution to this problem is presented in Fig. 3 and was obtained using the finite element mesh shown in Fig. 2b, with 1115 nodes and 3200 elements.

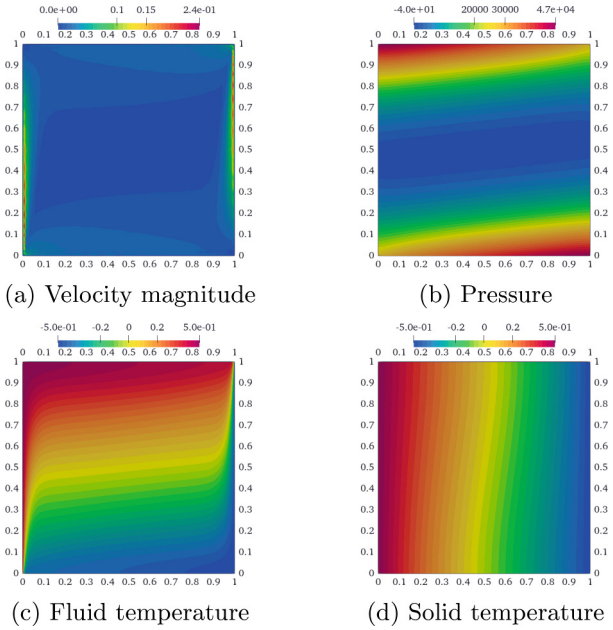

(a) Velocity magnitude (b) Pressure

(c) Fluid temperature (d) Solid temperature

Fig. 3. Solutions of the heated porous cavity application at $t = 250$.

A reference nondimensional pressure is set to $p_{ref} = 1$ at the central point of the cavity $C = (0.5, 0.5)$. The dimensionless time step is $\Delta t = 1$ and Table 4 shows the remain set of parameters used in the numerical solver.

Table 4. Parameters of the heated porous cavity with $L = 1\,\mathrm{m}$

		Re_L	Re_k	Da	ϕ	Nu	Ri
Type	**Regime**	$\rho \mathbf{u} L/\mu$	$\rho \mathbf{u}\sqrt{k}/\mu$	k/L^2	V_p/V	$f(Re_k, Pr, \phi)$	$\mathbf{g}\beta\Delta T L/{u_\infty}^2$
B	Darcy	1000	3.14×10^{-2}	9.87×10^{-10}	0.8	2.05	3.30×10^5

Despite the problem's porous nature, the thermal profiles are similar to those of classical solutions for free-flow problems. Due to buoyancy-driven fluid circulation, the temperature profile of the porous solid matrix deviates slightly from that of a quiescent (no-flow) scenario.

4.3 Thermal Fingers

A variation of the differentially heated cavity for a porous medium is shown in Fig. 4. The same set of parameters listed in Table 4 and reference pressure at the

central point is adopted in this case. The objective is to evaluate the stabilization performance in a more complex flow configuration with multiple thermal circulation cells. The domain is discretized using an alternating triangular mesh with 7803 nodes and 15000 elements. The dimensionless time step is set to $\Delta t = 1$, and the simulation is advanced up to $t = 25$, yielding a clear visualization of the convection cells.

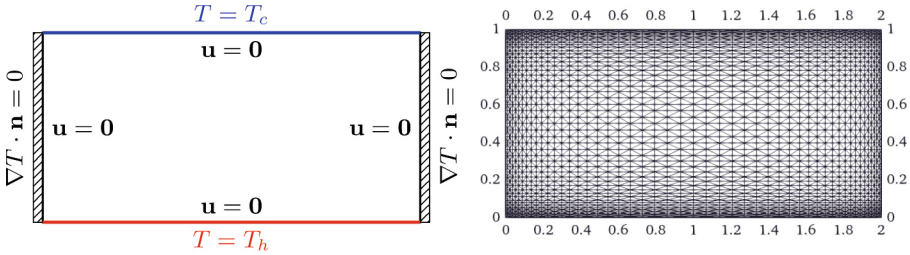

(a) Geometry and boundary conditions (b) Finite element mesh

Fig. 4. Porous thermal fingers application.

The results shown in Fig. 5 indicate that the method accurately captures the interaction between buoyancy-driven flow and thermal transport. In particular, the preservation of the thermal fingers (see Fig. 5c) and the symmetry of the

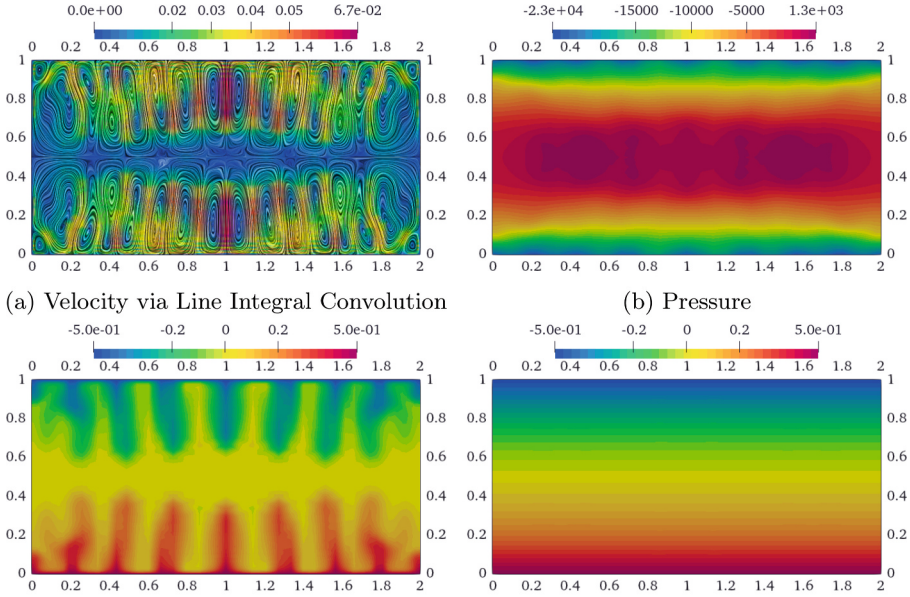

(a) Velocity via Line Integral Convolution (b) Pressure

(c) Fluid temperature (d) Solid temperature

Fig. 5. Solutions of the porous thermal fingers application at $t = 25$.

circulation patterns (see Fig. 5a) up to this time step highlight the method's capability to resolve complex flow structures. The transient evolution further demonstrates the robustness of the formulation under strongly convective conditions, where standard Galerkin methods can produce spurious oscillations. The solution remains stable throughout the simulation, with coherent flow patterns and no evidence of non-physical artifacts.

4.4 Flow in Heterogeneous Fractured Media

The last application considers a porous medium with spatially heterogeneous properties derived from a fractal-based field. The underlying scalar field is obtained from the escape-time of a Julia set fractal, mapped onto the physical domain Ω, and scaled to represent values ranging from type A to type B rocks presented in Table 2. This procedure introduces highly heterogeneous transport pathways that aim to mimic natural fractured or channelized structures.

The fractal field is generated using the standard quadratic iteration

$$z_{n+1} = z_n^2 + c \quad \text{for} \quad z \in \mathbb{C}, \tag{35}$$

with $c = -i$, corresponding to the Julia set $J(0, -i)$. The associated escape-time function is defined as

$$T(z) = \min \{n \in \mathbb{N} : |z_n| > R\}, \tag{36}$$

which assigns to each point $z \in \mathbb{C}$ the number of iterations required to exceed a prescribed escape radius R. To construct the fractal field over the physical domain, let $(x, y) \in \Omega = [0, 1]^2 \subset \mathbb{R}^2$ denote the spatial coordinates. We define the affine mapping

$$\zeta(x, y) = (4x - 2) + i(4y - 2), \tag{37}$$

which maps points from Ω to the complex plane region $[-2, 2] \times [-2, 2] \subset \mathbb{C}$ that contains the complete structure of the set $J(0, -i)$. The fractal field is then defined through the composition

$$F(x, y) = \mathcal{N}\big(T(\zeta(x, y))\big), \tag{38}$$

where $\mathcal{N}(\cdot)$ denotes a normalization operator mapping the escape-time values to the interval associated with type A and type B rocks. The resulting scalar field $F(x, y)$ is subsequently used to define the permeability, porosity, Forchheimer coefficient, and thermal conductivity distributions through appropriate scaling relations.

After $n = 15$ iterations using an escape radius $R = 10$, the resulting nondimensional permeability field is presented in Fig. 6b. Complex patterns characterized by branching structures and sharp transitions are clearly observed. These spatial features are directly reflected in the permeability, porosity, Forchheimer coefficient, and thermal conductivity fields, resulting in pronounced heterogeneity in both flow resistance and heat transfer.

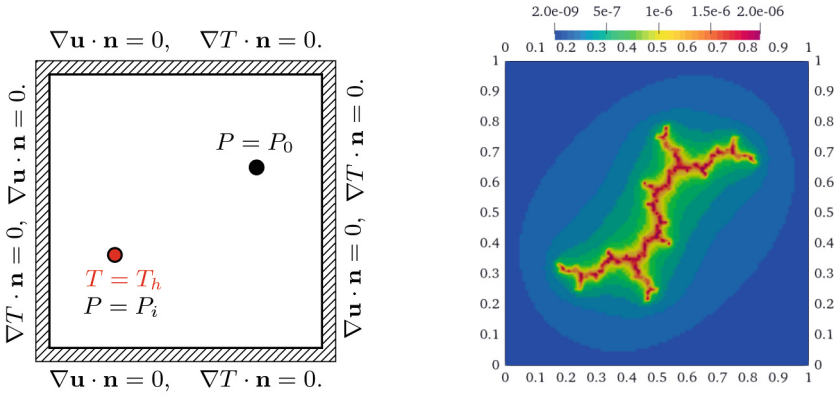

(a) Geometry and boundary conditions

(b) Da field from $J(0, -i)$

Fig. 6. Julia fractal fracture application.

Figure 6a shows the geometry of the problem and the chosen boundary conditions. The internal points indicate a source (red) at $I = (0.24, 0.34)$ and a sink (black) at $P = (0.76, 0.66)$, with pressures set to $p = 1.2$ and $p = 0.8$, respectively, creating a pressure gradient that drives the flow. A thermal gradient is induced by fixing the nondimensional temperature at the injection point I at $T_I = 0.5$, and the rest of the domain set to a lower value of $T = -0.5$.

The Reynolds number is set to 1000, and the problem is solved using an alternating triangular mesh with 10201 nodes and 20000 elements. The velocity field, presented in Fig. 7a, shows that the flow is strongly guided by the high-permeability channels defined by the fractal structure. Preferential flow paths emerge, forming localized high-velocity regions where non-Darcy effects occur.

The pressure field, shown in Fig. 7b, exhibits a smooth global gradient ranging between the fixed source and sink values with local distortions due to heterogeneous resistance.

Thermally, both fluid and solid temperatures, Figs. 7c and 7d, present localized hot spots near the injection region, with LTNE effects appearing as slight deviations between the two fields, especially along dominant flow paths where convection is enhanced.

4.5 Discussion of Results

The proposed stabilized finite element framework demonstrated robust and consistent performance across all investigated flow regimes. The combination of SUPG, PSPG, and LSIC stabilization enabled stable solutions under advection-dominated and non-Darcy conditions, without spurious oscillations typically associated with standard Galerkin formulations.

The use of equal-order linear interpolation for all primitive variables represents a practical advantage of the formulation. While a slightly higher error

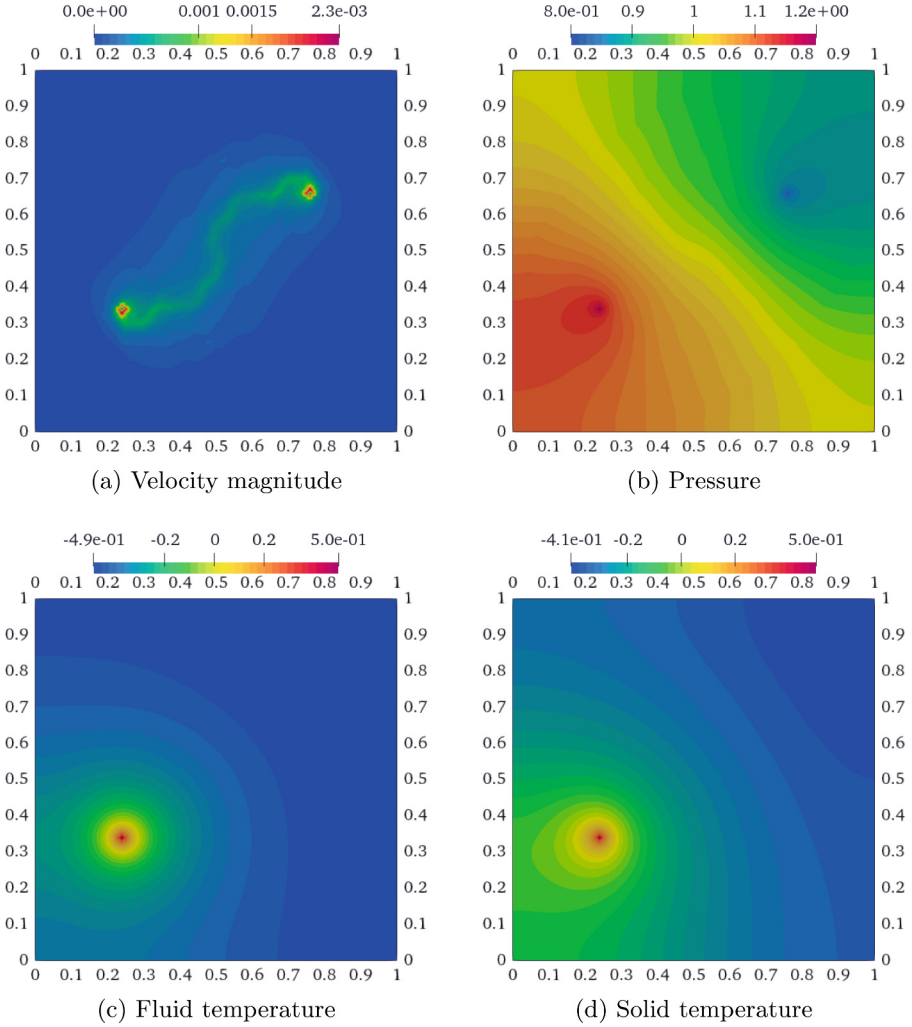

(a) Velocity magnitude (b) Pressure

(c) Fluid temperature (d) Solid temperature

Fig. 7. Solutions of the Julia fracture problem at $t = 200$.

is observed in the pressure field during the verification test, the PSPG stabilization ensures overall numerical stability and acceptable accuracy, providing a favorable balance between implementation simplicity and solution quality.

Although no direct comparison with alternative numerical methods is presented, the implementation's accuracy is supported by the manufactured solution test, which verifies the correct reproduction of the governing equations. Additionally, the benchmark applications exhibit physically consistent behavior, reinforcing the reliability of the proposed approach.

The results also highlight the formulation's ability to handle transitions between different flow regimes within a unified framework. The inclusion of

the Forchheimer term allows the capture of inertial effects at higher pore-scale Reynolds numbers, while the Brinkman term ensures a smooth transition toward viscous-dominated behavior.

Finally, the fractal-based permeability field naturally induces channelized flow patterns, demonstrating the method's ability to handle highly heterogeneous domains. The resulting flow and thermal fields exhibit strong spatial variability, consistent with expected behavior in fractured porous media.

5 Conclusions

In this work, a stabilized finite element framework for the transient DBF model coupled with a local thermal non-equilibrium formulation was presented. The approach combines SUPG, PSPG, and LSIC stabilization techniques within an equal-order interpolation setting, enabling a fully coupled and computationally efficient formulation.

The proposed method demonstrated stability and accuracy across different flow regimes, including advection-dominated and non-Darcy conditions. The verification study confirmed the correctness of the numerical implementation, while the benchmark applications showed physically consistent behavior in both thermal and flow fields.

The formulation successfully captures transitions between Darcy, Brinkman, and Forchheimer regimes without requiring model switching. In addition, the LTNE approach allows the resolution of thermal non-equilibrium effects between the fluid and solid phases, particularly in regions with strong convective transport.

The application to a fractal-based heterogeneous medium further demonstrated the method's ability to handle complex spatial variability, producing realistic channelized flow patterns and localized thermal effects.

Future work includes extending to three-dimensional configurations, investigating the tuning of stabilization parameters, applying other stabilization techniques, and evaluating GMRES and preconditioning options to improve performance.

Acknowledgments. This study was financed in part by the Coordenação de Aperfeiçoamento de Pessoal de Nível Superior - Brasil (CAPES) - Finance Code 001 - and by the Fundação de Amparo à Pesquisa e Inovação do Espírito Santo (FAPES), Grant Notice N° 02/2026.

Declaration of Generative AI and AI-Assisted Technologies in the Writing Process. During the preparation of this work the authors used ChatGPT (OpenAI) in order to assist with language revision and text improvement. After using this tool, the authors reviewed and edited the content as needed and take full responsibility for the content of the publication.

References

1. Akolkar, A., Petrasch, J.: Tomography-based characterization and optimization of fluid flow through porous media. Transp. Porous Media **95**(3), 535–550 (2012)
2. Baptista, R., dos Santos, I.P., Catabriga, L.: Solving incompressible Navier-stokes equations: a nonlinear multiscale approach. Comput. Math. Appl. **175**, 366–384 (2024)
3. Barnsley, M.F., et al.: The Science of Fractal Images, vol. 1. Springer, New York (1988). https://doi.org/10.1007/978-1-4612-3784-6
4. Berre, I., Doster, F., Keilegavlen, E.: Flow in fractured porous media: a review of conceptual models and discretization approaches. Transp. Porous Media **130**(1), 215–236 (2019)
5. Brezzi, F.: On the existence, uniqueness and approximation of saddle-point problems arising from Lagrangian multipliers. Publications des séminaires de mathématiques et informatique de Rennes **8**(R2), 129–151 (1974)
6. Brinkman, H.C.: A calculation of the viscous force exerted by a flowing fluid on a dense swarm of particles. Flow Turbul. Combust. **1**(1), 27–34 (1949)
7. Brooks, A.N., Hughes, T.J.: Streamline upwind/Petrov-Galerkin formulations for convection dominated flows with particular emphasis on the incompressible Navier-stokes equations. Comput. Methods Appl. Mech. Eng. **32**(1), 199–259 (1982)
8. Cannon, J.: The fractal geometry of nature. by benoit b. mandelbrot. Am. Math. Mon. **91**(9), 594–598 (1984)
9. Cengizci, S.: A sups formulation for simulating unsteady natural/mixed heat convection phenomena in square cavities under intense magnetic forces. Eur. Phys. J. Plus **139**(8), 713 (2024)
10. Darcy, H.: Les fontaines publiques de la ville de Dijon, vol. 2. V. Dalmont (1856)
11. Donea, J., Huerta, A.: Finite Element Methods for Flow Problems. Wiley, New York (2003)
12. Ern, A., Guermond, J.L.: Finite elements iii. first-order and time-dependent PDEs. Texts Appl. Math **74** (2021)
13. Forchheimer, P.: Wasserbewegung durch boden. Z. Ver. Deutsch, Ing. **45**, 1782–1788 (1901)
14. García-Garrido, V.J.: Unveiling the fractal structure of Julia sets with Lagrangian descriptors. Commun. Nonlinear Sci. Numer. Simul. **91**, 105417 (2020)
15. Geuzaine, C., Remacle, J.F.: GMSH: a 3-D finite element mesh generator with built-in pre-and post-processing facilities. Int. J. Numer. Meth. Eng. **79**(11), 1309–1331 (2009)
16. Gray, D.D., Giorgini, A.: The validity of the Boussinesq approximation for liquids and gases. Int. J. Heat Mass Transf. **19**(5), 545–551 (1976)
17. Hughes, T.J.: A multidimensional upwind scheme with no crosswind diffusion. Finite element methods for convection dominated flows. AMD **34** (1979)
18. Hughes, T.J., Mallet, M., Akira, M.: A new finite element formulation for computational fluid dynamics: Ii. beyond supg. Comput. Methods Appl. Mech. Eng. **54**(3), 341–355 (1986)
19. Kuwahara, F., Shirota, M., Nakayama, A.: A numerical study of interfacial convective heat transfer coefficient in two-energy equation model for convection in porous media. Int. J. Heat Mass Transf. **44**(6), 1153–1159 (2001)
20. Lemmon, E.W.: Thermophysical properties of fluid systems. NIST Chemistry WebBook (2010)

21. Macdonald, I., El-Sayed, M., Mow, K., Dullien, F.: Flow through porous media - the Ergun equation revisited. Ind. Eng. Chem. Fundam. **18**(3), 199–208 (1979)
22. de Moura, R.C., Catabriga, L.: Stabilized finite element approximation for the transient Darcy-Brinkman-Forchheimer model. In: 2023 IEEE 22nd International Conference on Trust, Security and Privacy in Computing and Communications (TrustCom), pp. 2357–2364. IEEE (2023)
23. Nield, D.A., Bejan, A.: Convection in Porous Media. Springer, Cham (2006). https://doi.org/10.1007/978-3-319-49562-0
24. Schön, J.H.: Physical Properties of Rocks: Fundamentals and Principles of Petrophysics, vol. 65. Elsevier, Amsterdam (2015)
25. Tezduyar, T.E.: Stabilized finite element formulations for incompressible flow computations. Adv. Appl. Mech. **28**, 1–44 (1991)
26. Tezduyar, T.E.: Calculation of the stabilization parameters in SUPG and PSPG formulations. Mecanica Computacional, 1–18 (2002)
27. Tezduyar, T.E., Mittal, S., Ray, S., Shih, R.: Incompressible flow computations with stabilized bilinear and linear equal-order-interpolation velocity-pressure elements. Comput. Methods Appl. Mech. Eng. **95**(2), 221–242 (1992)
28. Tezduyar, T.E., Osawa, Y.: Finite element stabilization parameters computed from element matrices and vectors. Comput. Methods Appl. Mech. Eng. **190**(3–4), 411–430 (2000)
29. Ward, J.: Turbulent flow in porous media. J. Hydraul. Div. **90**(5), 1–12 (1964)
30. Whitaker, S.: Diffusion and dispersion in porous media. AIChE J. **13**(3), 420–427 (1967)
31. Yu, T., Paradis, A.: On the simulation of artificial cracks in brittle materials using Julia set fractals. Multiscale Sci. Eng. **6**(4), 218–236 (2024)